The enhanced local pressure model for the accurate analysis of fluid pressure driven fracture in porous materials

E.W. Remij, J.J.C. Remmers*, J.M. Huyghe, D.M.J. Smeulders

Department of Mechanical Engineering, Eindhoven University of Technology, PO BOX 513, 5600 MB, Eindhoven, The Netherlands

Highlights

- A novel partition of unity based model is developed to simulate crack growth in porous materials.
- Fluid pressure in the crack is taken as an additional variable.
- High pressure gradients near cracks are resolved accurately.
- Hydraulic fracturing can be simulated by directly prescribing fluid flow in the crack.

Abstract

In this paper, we present an enhanced local pressure model for modelling fluid pressure driven fractures in porous saturated materials. Using the partition-of-unity property of finite element shape functions, we describe the displacement and pressure fields across the fracture as a strong discontinuity. We enhance the pressure in the fracture by including an additional degree of freedom. The pressure gradient due to fluid leakage near the fracture surface is reconstructed based on Terzaghi's consolidation solution. With this numerical formulation we ensure that all fluid flow goes exclusively in the fracture and it is not necessary to use a dense mesh near the fracture to capture the pressure gradient. Fluid flow in the rock formation is described by Darcy's law. The fracture process is governed by a cohesive traction–separation law. The performance of the numerical model for fluid driven fractures is shown in three numerical examples.
© 2015 Elsevier B.V. All rights reserved.

1. Introduction

Hydraulic fracturing is defined as the process by which a fracture propagates due to hydraulic loading, i.e., by applying a fluid pressure inside the fracture. In geo-mechanics, this process is applied to stimulate oil and gas reservoirs by injecting a highly viscous fluid into the underground formation. Once the induced fractures have sufficient width, a proppant is added to the fluid. After the release of the pumping pressure, the induced fractures

remain open under the highly confining stress due to the proppant and therefore greatly enhance the permeability of the reservoir [1]. Other applications of hydraulic fracturing include heat production from geothermal reservoirs [2] and measurements of in situ stresses [3]. A model to predict the hydraulic fracturing process can be used to optimize these processes. However, the correct modelling of the hydraulic fracturing process is complex since three different phenomena have to be taken into account: (i) the fluid exchange between the fracture and the rock formation (ii) the fluid flow in the fracture and (iii) the changing spatial configuration due to fracture propagation [1].

The first theoretical hydraulic fracture models were developed in the 1950s [4]. Perkins and Kern [5] developed a theoretical model based on the classic Sneddon plane strain crack propagation. Fluid loss was included in this model by Nordgren [6] and is now referred to as the PKN model. Similar models with slightly different geometrical assumptions were independently developed by Geertsma and de Klerk [7] and Khristianovic and Zheltov [8]. These models have been used for analysing several parameters that control hydraulic fracturing. This research has shown that hydraulic fracturing can be categorized in a parametric space based on hydraulic fractures that are dominated by fluid leak-off, toughness, or viscosity. Several asymptotic solutions are derived in this parametric space. An overview of these solutions is given by Adachi et al. [4].

Various numerical models have been developed for complex geometries where the analytical solutions fail. Boone and Ingraffea [9] developed a numerical model based on the finite element method (FEM) for the poroelastic material where a cohesive zone description was used for the fracture. The fluid flow in the crack was solved using a finite difference method. Schrefler and co-workers [10–12] modelled a cohesive fracture using the FEM but included a mesh adaptation scheme so that propagating fractures in arbitrary directions can be modelled in two- and three-dimensional situations. Hydraulic fracturing was investigated in a permeable material by Sarris and Papanastasiou [13] with a finite element analysis including cohesive zone elements. Segura and Carol [14,15] introduced a hydro-mechanical coupling formulation using zero-thickness interface elements with double nodes based on the FEM. Carrier and Granet [16] also used interface elements but included an additional degree of freedom for the pressure in the fracture. Recently, also advancements were made in continuum based hydraulic fracturing simulations using a phase-field approach [17].

The eXtended Finite Element Method (X-FEM) is a proven technology in solid mechanics and has as an important advantage compared to the previously mentioned fracture models; a fracture can grow in arbitrary directions without the need to remesh [18]. In X-FEM a fracture is modelled as a discontinuity in the displacement field by exploiting the partition-of-unity property of finite element shape functions [19]. Black and Belytschko [20] and Moës et al. [21] were the first to implement this in the FEM by adding additional degrees of freedom to the existing nodes in the finite element mesh. A cohesive zone description for the fracture process was included by Wells and Sluys [22]. The X-FEM was successfully applied to fracturing in porous materials, see e.g. [23–25]. Recently, Mohammadnejad and Khoei [26] developed a X-FEM model for cohesive crack growth in multiphase porous materials. They successfully applied their model for hydraulic fracturing simulations [27]. In these works the pressure field across the fracture is enriched with a linear distance function. This leads to a continuous pressure description across the fracture while the fluid flow is discontinuous. In this paper, we use this model for benchmarking purposes and refer to it as the continuous pressure X-FEM model.

A drawback of a continuous pressure description is that an inflow, as present in hydraulic fracturing, must be prescribed as a boundary condition of the continuous external fluid flow. Therefore, a mesh dependent part of the fluid flow goes directly in the formation instead of into the fracture. This effect decreases in an opened fracture due to the high permeability in the fracture compared with the rock formation. However, the effect may be significant in an initial closed fracture, particularly when the mesh is coarse. A second drawback of a continuous pressure over the fracture is that a sufficiently fine mesh near the fracture is necessary to capture the pressure gradient. The length-scale of the gradient decreases with a decreasing intrinsic permeability. Therefore, this effect may be severe in low permeable rocks such as shales.

To quantify these effects, we develop a model with an additional, separate, degree of freedom for the fluid pressure in the fracture. By doing this, we ensure that the inflow goes exclusively into the fracture. The fluid leaks off into the formation only from the fracture itself. We enrich the pressure, as we do for the displacement field, with a Heaviside function, making the pressure discontinuous over the fracture. Hence, the pressure exhibits a jump for the fracture to the formation on the left and another jump for the fracture to the formation on the right as in Fig. 1. The steep pressure gradients along the boundaries of the fracture are therefore not resolved. The steep gradients along the boundaries of the fracture are reconstructed assuming a scale separation between on the one hand the consolidation phenomenon around the fracture, and on the other hand the macroscopic fluid flow in the formation. The consolidation phenomenon
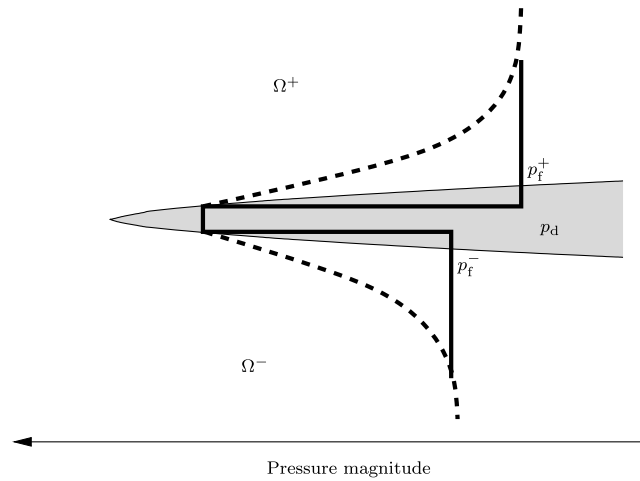
Fig. 1. Schematic representation of the pressure magnitude over an open discontinuity in grey. The discontinuity separates the formation into two bodies, Ω^+ and Ω^-, with a pressure p_f^+ and p_f^-, respectively. The pressure in the discontinuity is given by p_d. The striped line indicates the physical pressure gradient over the discontinuity. The solid line represents the discontinuous pressure profile.

itself is reconstructed from an one-dimensional analytical solution based on Terzaghi's consolidation equation [28]. The numerical model is only valid when the characteristic distance of consolidation around the fracture is small relative to the mesh-size of the formation. We will refer to this model as the Enhanced Local Pressure (ELP) model. The pressure near the fracture can be compared to an one-dimensional analytical solution. By comparing the ELP model and the continuous X-FEM formulation with the analytical solution we investigate if indeed the ELP model better approximates the pressure in the fracture at small distance-scales.

In the remainder of this paper we first describe the kinematic relations. In Section 3 we present the balance equations and in Section 4 the governing equations are introduced. The weak form is given in Section 5 and the discretization and numerical implementation are given in Section 6. In Section 7 we illustrate the performance of the model with three examples. Finally, we draw our conclusions in Section 8.

2. Kinematic relations

Consider a body Ω crossed by a discontinuity Γ_d, as shown in Fig. 2(a). The discontinuity divides the body in two domains, Ω^+ and Ω^-. The vector $\mathbf{n}_d$ is defined as the normal of the discontinuity surface Γ_d pointing into domain Ω^+. The total displacement field of the solid skeleton can, at any time t, be described by a regular displacement field $\hat{\mathbf{u}}(\mathbf{x}, t)$ and an additional displacement field $\tilde{\mathbf{u}}(\mathbf{x}, t)$ [20,21,29]

$$\mathbf{u}(\mathbf{x}, t) = \hat{\mathbf{u}}(\mathbf{x}, t) + \mathcal{H}_{\Gamma_d}(\mathbf{x})\tilde{\mathbf{u}}(\mathbf{x}, t), \tag{1}$$

where $\mathbf{x}$ is the position of a material point and $\mathcal{H}_{\Gamma_d}$ is the Heaviside step function. Across the discontinuity, this is defined as

$$\mathcal{H}_{\Gamma_d} = \begin{cases} 1 & \text{if } \mathbf{x} \in \Omega^+ \\ 0 & \text{if } \mathbf{x} \in \Omega^-. \end{cases} \tag{2}$$

The strain field results from differentiating the displacement field (1) with respect to material point $\mathbf{x}$ with the assumption of small strain theory

$$\boldsymbol{\epsilon}(\mathbf{x}, t) = \nabla^s \hat{\mathbf{u}}(\mathbf{x}, t) + \mathcal{H}_{\Gamma_d} \nabla^s \tilde{\mathbf{u}}(\mathbf{x}, t), \quad \mathbf{x} \notin \Gamma_d. \tag{3}$$

Here ∇^s is the symmetric part of the differential operator

$$\nabla^s \mathbf{u} = \frac{1}{2}(\nabla \mathbf{u} + (\nabla \mathbf{u})^T). \tag{4}$$
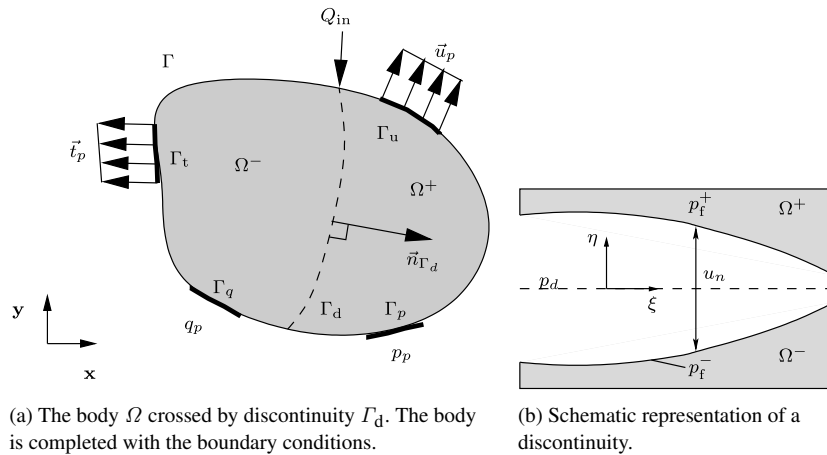
(a) The body Ω crossed by discontinuity Γ_d. The body is completed with the boundary conditions.

(b) Schematic representation of a discontinuity.

Fig. 2. Schematic representation of body Ω and of a discontinuity.

At the discontinuity Γ_d, the strain field is undefined and the kinematic quantity is defined by a jump in the displacement field

$$\mathbf{v}_\mathrm{d}(\mathbf{x}, t) = \tilde{\mathbf{u}}(\mathbf{x}, t), \quad \mathbf{x} \in \Gamma_\mathrm{d}. \tag{5}$$

The pressure inside an opening fracture is different from the pressure inside the surrounding formation. The gradient of this pressure difference quantifies the interaction of fluid flow between the fracture and the formation. We assume the pressure to be discontinuous across the fracture:

$$p(\mathbf{x}, t) = \hat{p}(\mathbf{x}, t) + \mathcal{H}_{\Gamma_\mathrm{d}}(\mathbf{x}) \tilde{p}(\mathbf{x}, t). \tag{6}$$

In the discontinuity, the pressure is equal to an independent variable p_d (Fig. 2(b)).

$$p_\mathrm{d} = p \quad \mathbf{x} \in \Gamma_\mathrm{d}. \tag{7}$$

3. Balance equations

The balance equations consist of two parts, namely balance equations in the bulk material and on a more local scale inside the fracture. These two types are identified separately in this section.

3.1. Bulk behaviour

The porous solid skeleton is considered to be fully saturated with a fluid. The process is isothermal and gravity, inertia, body forces, and convection are neglected. With these assumptions the momentum balance reads

$$\nabla \cdot \boldsymbol{\sigma} = \mathbf{0}, \tag{8}$$

where $\boldsymbol{\sigma}$ is the total stress which is decomposed in Terzaghi's effective stress $\boldsymbol{\sigma}_\mathrm{e}$ and the hydrostatic pressure p [28]

$$\boldsymbol{\sigma} = \boldsymbol{\sigma}_\mathrm{e} - \alpha p \mathbf{I}, \tag{9}$$

with $\mathbf{I}$ the unit matrix and α the Biot coefficient

$$\alpha = 1 - \frac{K}{K_\mathrm{s}}. \tag{10}$$

Here, K and K_s are the bulk moduli of the porous material and the solid constituent, respectively. The momentum balance is completed with the following boundary conditions (Fig. 2(a))

$$\begin{aligned}
\boldsymbol{\sigma} \cdot \mathbf{n}_\Gamma &= \mathbf{t}_\mathrm{p}(\mathbf{x}, t) \quad \mathbf{x} \in \Gamma_t, \\
\mathbf{u}(\mathbf{x}, t) &= \mathbf{u}_\mathrm{p}(\mathbf{x}, t) \quad \mathbf{x} \in \Gamma_u,
\end{aligned} \tag{11}$$

with $\Gamma_t \cup \Gamma_u = \Gamma, \Gamma_t \cap \Gamma_u = \emptyset$.

We neglect mass transfer between the two constituents. The mass balance is written as [24]

$$\alpha \nabla \cdot \mathbf{v}_{\mathrm{s}} + \nabla \cdot \mathbf{q} + \frac{1}{M} \dot{p} = 0, \tag{12}$$

where $\mathbf{v}_{\mathrm{s}}$ is the deformation velocity of the solid skeleton, $\mathbf{q}$ is the seepage flux, and M is the compressibility modulus defined as

$$\frac{1}{M} = \frac{\phi}{K_{\mathrm{f}}} + \frac{1-\phi}{K_{\mathrm{s}}}. \tag{13}$$

Here ϕ is the porosity of the porous material and K_{f} is the bulk modulus of the fluid. The mass balance is completed with the following boundary conditions (Fig. 2(a))

$$\begin{aligned}
\mathbf{q}(\mathbf{x}, t) \cdot \mathbf{n}_{\Gamma} &= q_{\mathrm{p}} \quad \mathbf{x} \in \Gamma_q, \\
p(\mathbf{x}, t) &= p_{\mathrm{p}} \quad \mathbf{x} \in \Gamma_p,
\end{aligned} \tag{14}$$

with $\Gamma_q \cup \Gamma_p = \Gamma, \Gamma_q \cap \Gamma_p = \emptyset$.

3.2. Microscopic model

Following a cohesive zone approach, the softening of the material is governed by a traction acting on the discontinuity surface. This traction is coupled to the hydrostatic pressure in the discontinuity. Assuming continuity of stress from the continuum into the discontinuity, we can write the local momentum balance as

$$\boldsymbol{\sigma} \cdot \mathbf{n}_{\mathrm{d}} = \mathbf{t}_{\mathrm{d}} - p_{\mathrm{d}} \mathbf{n}_{\mathrm{d}}. \tag{15}$$

The local mass balance in the discontinuity can be found by integrating the continuous mass balance across the discontinuity.

$$\left(\mathbf{q}_{\Gamma_{\mathrm{d}}}^{+} - \mathbf{q}_{\Gamma_{\mathrm{d}}}^{-}\right) \cdot \mathbf{n}_{\mathrm{d}} + \dot{u}_n + u_n \left\langle \frac{\partial \dot{u}_s}{\partial s} \right\rangle - u_n \frac{\partial}{\partial s}\left(k_{\mathrm{d}} \frac{\partial p_{\mathrm{d}}}{\partial s}\right) + \frac{u_n}{K_f} \dot{p}_{\mathrm{d}} = 0, \tag{16}$$

with $\mathbf{q}_{\Gamma_{\mathrm{d}}}^{+}$ and $\mathbf{q}_{\Gamma_{\mathrm{d}}}^{-}$ being the fluid flow from the discontinuity into formation for the discontinuity lip of the Ω^{+} and the Ω^{-} domain, respectively, $\dot{u}_n$ denoting the time derivative of the normal opening of the discontinuity, u_s being the shear opening of the discontinuity, $\langle \cdot \rangle = \frac{\cdot^{+} + \cdot^{-}}{2}$ describing the average across the discontinuity, and k_{d} being the permeability in the discontinuity. The latter is given by [30]:

$$k_{\mathrm{d}} = \frac{u_n^2}{12\mu}, \tag{17}$$

where μ is the viscosity of the fluid. For the derivation of this equilibrium equation, we refer to Irzal et al. [23].

4. Constitutive equations

The mathematical formulation of the balance equations are completed by constitutive behaviour for the bulk material and the discontinuity.

4.1. Mechanical behaviour of the bulk

The effective stress in the bulk material is related to the strain with a linear reversible stress–strain relation:

$$\boldsymbol{\sigma}_{\mathrm{e}} = 2\mu\boldsymbol{\epsilon} + \lambda\mathrm{tr}(\boldsymbol{\epsilon})\mathbf{I}, \tag{18}$$

where μ and λ are respectively the first and second Lamé constants given in an isotropic material by

$$\mu = \frac{E}{2(1+\nu)} \qquad \lambda = \frac{\nu E}{(1+\nu)(1-2\nu)}, \tag{19}$$

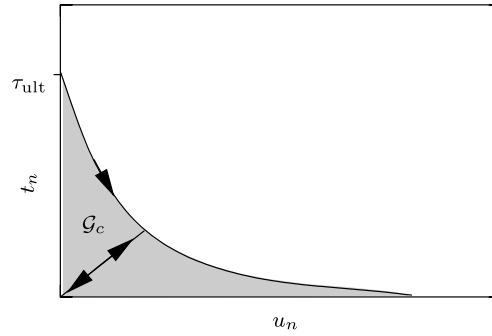with E and ν being the Young's modulus and the Poisson's ratio, respectively.

Fig. 3. Exponential traction–separation law.

The fluid flow in the bulk material can be described by Darcy's relation [31]

$$\mathbf{q} = -\boldsymbol{k} \cdot \nabla p, \tag{20}$$

where $\boldsymbol{k}$ is the permeability tensor, $\boldsymbol{k} = k\mathbf{I}$, of the porous material. The permeability k is assumed to be isotropic and constant in time and space [32].

4.2. Mechanical behaviour in the discontinuity

The constitutive mechanical behaviour at the discontinuity is given by a relationship between the traction at the interface and the displacement jump $\mathbf{u}_d$ across the discontinuity [23]:

$$\mathbf{t}_d = \mathbf{t}_d(\mathbf{u}_d, \kappa). \tag{21}$$

Here κ is a history parameter that is equal to the largest displacement jump reached. It is necessary to perform a linearization on Eq. (21) in order to use the tangential stiffness matrix in an incremental iterative solution:

$$\Delta \mathbf{t}_d = \mathbf{T} \Delta \mathbf{u}_d. \tag{22}$$

The relation between the traction $\mathbf{t}_d$ and the displacement jump $\mathbf{u}_d$ can be any traction–separation relation and is referred to as the cohesive law. We assume that the fluid pressure inside the hydraulic fractures only causes fracture opening in normal direction. Therefore, shear tractions are neglected and we use an exponential cohesive law that is only a function of normal opening u_n (Fig. 3)

$$t_n = \tau_{\text{ult}} \exp\left(-\frac{u_n \tau_{\text{ult}}}{\mathcal{G}_{\text{c}}}\right). \tag{23}$$

Here is τ_{ult} the ultimate strength of the material and $\mathcal{G}_{\text{c}}$ the fracture toughness.

4.3. Small scale pressure coupling

Due to the discontinuous pressure formulation, the pressure gradient between the discontinuity and the formation is undetermined. If the consolidation distance is small compared to the dimensions of the finite elements near the discontinuity, we approximate the pressure gradient using the 1D analytical solution for a semi-infinite formation, given by Eq. (62) in Appendix A. In this analytical solution, the value p represents the pressure difference between the boundary surface and the initial pressure due to the loading of the formation. In the case of a discontinuity, there is a pressure gradient between the discontinuity and the formation, see Fig. 2(b). We therefore substitute p with this pressure difference. The fluid leakage is then taken from the analytical solution and thus given by

$$\mathbf{q} \cdot \mathbf{n} = Q_{\text{in}} = \frac{k}{2} \frac{p_d - p_f}{\sqrt{\frac{c_v t}{\pi}} \exp\frac{-\eta^2}{4c_v t} - \frac{\eta}{2}\text{erfc}\left(\frac{\eta}{2\sqrt{c_v t}}\right)}. \tag{24}$$

At the boundary of discontinuity, defined by $\eta = 0$, the fluid flow simplifies into

$$\mathbf{q} \cdot \mathbf{n} = \frac{k}{2} \frac{p_\mathrm{d} - p_\mathrm{f}}{\sqrt{\frac{c_v t}{\pi}}}. \tag{25}$$

Here p_f is the pressure in the formation at the edge of the fracture (Fig. 2(b)) and t is the time that expired after the discontinuity was inserted. The diffusion coefficient c_v is given by

$$c_v = kM \frac{K + \frac{4}{3}\mu}{K_u + \frac{4}{3}\mu}, \tag{26}$$

with K_u being the undrained bulk modulus

$$K_u = K + \alpha^2 M. \tag{27}$$

Taking the side of the discontinuity into consideration, we can write this equation as

$$\left(\mathbf{q}_{\Gamma_\mathrm{d}}^+ - \mathbf{q}_{\Gamma_\mathrm{d}}^-\right) \cdot \mathbf{n}_\mathrm{d} = C_\mathrm{a}\left(2p_\mathrm{d} - p_\mathrm{f}^+ - p_\mathrm{f}^-\right), \tag{28}$$

where the C_a is an analytical constant define by

$$C_\mathrm{a} = \frac{k}{2\sqrt{\frac{c_v t}{\pi}}}. \tag{29}$$

5. Weak form

The weak form of the previously derived equilibrium equations can be expressed by multiplying them with admissible test functions for each field variable. The test functions for the momentum balance and the mass balance have the same form as the displacement field u and the pressure field p, respectively:

$$\eta = \hat{\eta} + \mathcal{H}_{\Gamma_\mathrm{d}}\tilde{\eta} \qquad \zeta = \hat{\zeta} + \mathcal{H}_{\Gamma_\mathrm{d}}\tilde{\zeta}. \tag{30}$$

The pressure in the fracture p_d is continuous along the discontinuity and therefore multiplied by the test function ψ.

Multiplying the momentum balance (8) with the test function η, using Gauss's theorem and incorporating the boundary conditions, the weak momentum balance can be written as

$$\int_\Omega \nabla(\hat{\eta} + \mathcal{H}_{\Gamma_\mathrm{d}}\tilde{\eta}) : \boldsymbol{\sigma}\,\mathrm{d}\Omega = \int_{\Gamma_t} \nabla(\hat{\eta} + \mathcal{H}_{\Gamma_\mathrm{d}}\tilde{\eta})\mathbf{t}_\mathrm{p}\mathrm{d}\Gamma_t$$
$$- \int_{\Gamma_\mathrm{d}^+} \nabla(\hat{\eta} + \mathcal{H}_{\Gamma_\mathrm{d}}\tilde{\eta}) \cdot (\boldsymbol{\sigma} \cdot \mathbf{n}_\mathrm{d})\mathrm{d}\Gamma_\mathrm{d}^+ + \int_{\Gamma_\mathrm{d}^-} \nabla(\hat{\eta} + \mathcal{H}_{\Gamma_\mathrm{d}}\tilde{\eta}) \cdot (\boldsymbol{\sigma} \cdot \mathbf{n}_\mathrm{d})\mathrm{d}\Gamma_\mathrm{d}^-. \tag{31}$$

Multiplying the mass balance (12) with the test function ζ results in:

$$-\alpha \int_\Omega (\hat{\zeta} + \mathcal{H}_{\Gamma_\mathrm{d}}\tilde{\zeta})\nabla \cdot \mathbf{v}_\mathrm{s}\mathrm{d}\Omega + \int_\Omega \nabla(\hat{\zeta} + \mathcal{H}_{\Gamma_\mathrm{d}}\tilde{\zeta}) \cdot \mathbf{q}\mathrm{d}\Omega$$
$$- \int_\Omega (\hat{\zeta} + \mathcal{H}_{\Gamma_\mathrm{d}}\tilde{\zeta})\frac{1}{M}\frac{\partial p}{\partial t}\mathrm{d}\Omega = \int_{\Gamma_f} (\hat{\zeta} + \mathcal{H}_{\Gamma_\mathrm{d}}\tilde{\zeta})f_\mathrm{f}\mathrm{d}\Gamma. \tag{32}$$

Here we do not consider the fluid leakage. This term is included in the microscopic pressure coupling. The mass balance for the fluid flow in the fracture (16) is multiplied by test function ψ:

$$\int_{\Gamma_\mathrm{d}^+} \psi \mathbf{q}_{\Gamma_\mathrm{d}}^+ \cdot \mathbf{n}_\mathrm{d}\mathrm{d}\Gamma - \int_{\Gamma_\mathrm{d}^-} \psi \mathbf{q}_{\Gamma_\mathrm{d}}^- \cdot \mathbf{n}_\mathrm{d}\mathrm{d}\Gamma + \int_{\Gamma_\mathrm{d}} \psi\alpha\dot{u}_n\mathrm{d}\Gamma + \int_{\Gamma_\mathrm{d}} \psi u_n \left\langle \frac{\partial\dot{u}_s}{\partial s} \right\rangle \mathrm{d}\Gamma$$
$$+ \int_{\Gamma_\mathrm{d}} \psi \frac{u_n}{K_\mathrm{f}}\dot{p}_\mathrm{d}\mathrm{d}\Gamma - \int_{\Gamma_\mathrm{d}} \psi \frac{1}{12\mu}u_n^3 \frac{\partial}{\partial s}\frac{\partial p_\mathrm{d}}{\partial s}\mathrm{d}\Gamma = 0. \tag{33}$$

These two weak equations must hold for all variations of test functions and can therefore be solved separately for $(\tilde{\boldsymbol{\eta}} = 0, \tilde{\zeta} = 0)$ and for $(\hat{\boldsymbol{\eta}} = 0, \hat{\zeta} = 0)$. This results in the following four equations

$$\int_{\Omega} (\nabla \hat{\boldsymbol{\eta}}) : \boldsymbol{\sigma} \mathrm{d}\Omega = \int_{\Gamma_t} \hat{\boldsymbol{\eta}} \cdot \mathbf{t}_{\mathrm{p}} \mathrm{d}\Gamma, \tag{34}$$

$$\int_{\Omega} \mathcal{H}_{\Gamma_{\mathrm{d}}} \nabla \tilde{\boldsymbol{\eta}} : \boldsymbol{\sigma} \mathrm{d}\Omega + \int_{\Gamma_{\mathrm{d}}} \tilde{\boldsymbol{\eta}} \cdot (\mathbf{t}_{\mathrm{d}} - p_{\mathrm{d}}\mathbf{n}_{\mathrm{d}}) \mathrm{d}\Gamma = \int_{\Gamma_t} (\mathcal{H}_{\Gamma_{\mathrm{d}}} \tilde{\boldsymbol{\eta}}) \cdot \mathbf{t}_{\mathrm{p}} \mathrm{d}\Gamma, \tag{35}$$

$$-\alpha \int_{\Omega} \hat{\zeta} \nabla \cdot \mathbf{v}_{\mathrm{s}} \mathrm{d}\Omega + \int_{\Omega} \nabla \hat{\zeta} \cdot \mathbf{q} \mathrm{d}\Omega - \int_{\Omega} \hat{\zeta} \frac{1}{M} \frac{\partial p}{\partial t} \mathrm{d}\Omega = \int_{\Gamma_f} \hat{\zeta} f_{\mathrm{f}} \mathrm{d}\Gamma, \tag{36}$$

$$-\alpha \int_{\Omega} \mathcal{H}_{\Gamma_{\mathrm{d}}} \tilde{\zeta} \nabla \cdot \mathbf{v}_{\mathrm{s}} \mathrm{d}\Omega + \int_{\Omega} \mathcal{H}_{\Gamma_{\mathrm{d}}} \nabla \tilde{\zeta} \cdot \mathbf{q} \mathrm{d}\Omega - \int_{\Omega} \mathcal{H}_{\Gamma_{\mathrm{d}}} \tilde{\zeta} \frac{1}{M} \frac{\partial p}{\partial t} \mathrm{d}\Omega = \int_{\Gamma_f} \mathcal{H}_{\Gamma_{\mathrm{d}}} \tilde{\zeta} f_{\mathrm{f}} \mathrm{d}\Gamma. \tag{37}$$

Here we assumed stress continuity over the discontinuity ($\boldsymbol{\sigma} \cdot \mathbf{n}_{\mathrm{d}} = \mathbf{t}_{\mathrm{d}} - p_{\mathrm{d}}\mathbf{n}_{\mathrm{d}}$) and used the definition of the Heaviside function Eq. (2).

The fifth equilibrium equation, the mass balance for the fluid flow in the fracture (33), can be rewritten by using the divergence theorem in:

$$\int_{\Gamma_{\mathrm{d}}} \psi u \frac{1}{12\mu} u_n^3 \frac{\partial}{\partial s} \frac{\partial p_{\mathrm{d}}}{\partial s} \mathrm{d}\Gamma = \psi \frac{1}{12\mu} u_n^3 \frac{\partial p_{\mathrm{d}}}{\partial s} \bigg|_{S_{\mathrm{d}}} - \int_{\Gamma_{\mathrm{d}}} \frac{1}{12\mu} u_n^3 \frac{\partial \psi}{\partial s} \cdot \frac{\partial p_{\mathrm{d}}}{\partial s} \mathrm{d}\Gamma. \tag{38}$$

The term $\frac{1}{12\mu} u_n^3 \frac{\partial p_{\mathrm{d}}}{\partial s}|_{S_{\mathrm{d}}}$ represents the fluid inflow at the end of the fracture and is rewritten as

$$\frac{1}{12\mu} u_n^3 \frac{\partial p_{\mathrm{d}}}{\partial s} \bigg|_{S_{\mathrm{d}}} = Q_{\mathrm{in}}|_{S_{\mathrm{d}}}. \tag{39}$$

This gives the following relation for the mass balance in the discontinuity

$$\int_{\Gamma_{\mathrm{d}}} \psi \mathbf{q}_{\Gamma_{\mathrm{d}}}^+ \cdot \mathbf{n}_{\mathrm{d}} \mathrm{d}\Gamma - \int_{\Gamma_{\mathrm{d}}} \psi \mathbf{q}_{\Gamma_{\mathrm{d}}}^+ \cdot \mathbf{n}_{\mathrm{d}} \mathrm{d}\Gamma + \int_{\Gamma_{\mathrm{d}}} \psi \dot{u}_n \mathrm{d}\Gamma + \int_{\Gamma_{\mathrm{d}}} \psi u_n \left\langle \frac{\partial \dot{u}_s}{\partial s} \right\rangle \mathrm{d}\Gamma$$
$$+ \int_{\Gamma_{\mathrm{d}}} \psi \frac{u_n}{K_{\mathrm{f}}} \dot{p}_{\mathrm{d}} \mathrm{d}\Gamma + \int_{\Gamma_{\mathrm{d}}} \frac{1}{12\mu} u_n^3 \frac{\partial \psi}{\partial s} \cdot \frac{\partial p_{\mathrm{d}}}{\partial s} \mathrm{d}\Gamma = \psi Q_{\mathrm{in}}|_{S_{\mathrm{d}}}. \tag{40}$$

6. Discretization

The spatial discretization of the balance equations is based on the partition-of-unity property of finite element shape functions as described in the work of Babuška and Melenk [19]. The variational forms, the displacement field, the pressure field, and the pressure in the fracture are discretized similarly following the Bubnov–Galerkin approach for a single element by:

$$\begin{aligned}
\boldsymbol{\eta} &= \mathbf{N}\hat{\boldsymbol{\eta}} + \mathcal{H}_{\Gamma_{\mathrm{d}}}\mathbf{N}\tilde{\boldsymbol{\eta}}, & \mathbf{u} &= \mathbf{N}\hat{\mathbf{u}} + \mathcal{H}_{\Gamma_{\mathrm{d}}}\mathbf{N}\tilde{\mathbf{u}}, \\
\zeta &= \mathbf{H}\hat{\boldsymbol{\xi}} + \mathcal{H}_{\Gamma_{\mathrm{d}}}\mathbf{H}\tilde{\boldsymbol{\xi}}, & p &= \mathbf{H}\hat{\mathbf{p}} + \mathcal{H}_{\Gamma_{\mathrm{d}}}\mathbf{H}\tilde{\mathbf{p}}, \\
\psi &= \mathbf{V}\boldsymbol{\psi}, & p_{\mathrm{d}} &= \mathbf{V}\mathbf{p}_{\mathrm{d}},
\end{aligned} \tag{41}$$

where $\mathbf{N}$, $\mathbf{H}$, and $\mathbf{V}$ are matrices containing the standard shape functions for respectively, the nodal displacement, the pressure, and the pressure in the fracture for all nodes that support the element. Note that the shape functions for the nodal displacement and the pressure are two-dimensional functions while the pressure in fracture is described in an one-dimensional domain (Fig. 4). The columns $\hat{\mathbf{u}}$ and $\hat{\mathbf{p}}$ contain the continuous nodal values of respectively, the displacement and the pressure while $\tilde{\mathbf{u}}$ and $\tilde{\mathbf{p}}$ contain the values of the enhanced nodes. The column $\mathbf{p}_{\mathrm{d}}$ contains the nodal values of the pressure in the fracture. The discretized strain in the bulk can be derived by differentiation as

$$\boldsymbol{\epsilon} = \mathbf{B}\hat{\mathbf{u}} + \mathcal{H}_{\Gamma_{\mathrm{d}}}\mathbf{B}\tilde{\mathbf{u}}, \tag{42}$$
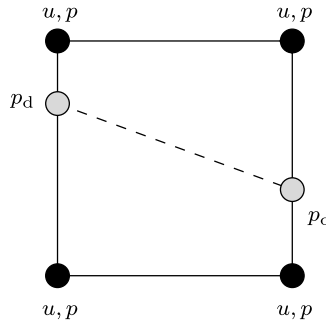
Fig. 4. Four nodal element with crossed by a discontinuity (dashed line).

where $\mathbf{B} = \mathbf{L}\mathbf{N}^T$ contains the spatial derivative of the standard shape functions. The differential matrix operator $\mathbf{L}$ is in the two-dimensional case defined as

$$\mathbf{L} = \begin{bmatrix} \dfrac{\partial}{\partial x} & 0 \\ 0 & \dfrac{\partial}{\partial y} \\ \dfrac{\partial}{\partial y} & \dfrac{\partial}{\partial x} \end{bmatrix}. \tag{43}$$

The discretized gradient of the pressure is defined as follows:

$$\nabla p = \nabla \mathbf{H}\hat{\mathbf{p}} + \mathcal{H}_{\Gamma_d} \nabla \mathbf{H}\tilde{\mathbf{p}}. \tag{44}$$

Inserting Eq. (41) into the weak form of the momentum balance and the mass balance yields in the following relations

$$\int_{\Omega_e} \mathbf{B}^T \boldsymbol{\sigma} \, d\Omega_e = \int_{\Gamma_t} \mathbf{N}^T \mathbf{t}_p \, d\Gamma, \tag{45}$$

$$\int_{\Omega_e} \mathcal{H}_{\Gamma_d} \mathbf{B}^T \boldsymbol{\sigma} \, d\Omega_e + \int_{\Gamma_d} \mathbf{N}^T (\mathbf{t}_d - \alpha p_d \mathbf{n}_d) d\Gamma = \int_{\Gamma_t} \mathcal{H}_{\Gamma_d} \mathbf{N}^T \mathbf{t}_p \, d\Gamma, \tag{46}$$

$$-\int_{\Omega} \alpha \mathbf{H}^T \mathbf{m}^T \nabla \dot{\mathbf{u}} \, d\Omega + \int_{\Omega} \nabla \mathbf{H}^T \mathbf{q} \, d\Omega - \int_{\Omega} \mathbf{H}^T \frac{1}{M} \dot{p} \, d\Omega = \int_{\Gamma_f} \mathbf{H}^T f_f \, d\Gamma, \tag{47}$$

$$-\int_{\Omega} \alpha \mathcal{H}_{\Gamma_d} \mathbf{H}^T \mathbf{m}^T \nabla \dot{\mathbf{u}} \, d\Omega + \int_{\Omega} \nabla \mathcal{H}_{\Gamma_d} \mathbf{H}^T \cdot \mathbf{q} \, d\Omega - \int_{\Omega} \frac{1}{M} \mathcal{H}_{\Gamma_d} \mathbf{H}^T \frac{\partial p}{\partial t} \, d\Omega$$

$$= \int_{\Gamma_f} \mathcal{H}_{\Gamma_d} \mathbf{H}^T f_f \, d\Gamma, \tag{48}$$

and for the mass balance in the fracture (40):

$$\int_{\Gamma_d^+} \mathbf{V}^T \left(\mathbf{q}_{\Gamma_d}^+ - \mathbf{q}_{\Gamma_d}^- \right) \cdot \mathbf{n}_d \, d\Gamma + \int_{\Gamma_d} \mathbf{V}^T \dot{u}_n \, d\Gamma + \int_{\Gamma_d} \mathbf{V}^T u_n \left\langle \frac{\partial \dot{u}_s}{\partial s} \right\rangle d\Gamma$$

$$+ \int_{\Gamma_d} \mathbf{V}^T \frac{u_n}{M_f} \dot{p}_d \, d\Gamma + \int_{\Gamma_d} \frac{1}{12\mu} u_n^3 \frac{\partial \mathbf{V}^T}{\partial s} \cdot \frac{\partial p_d}{\partial s} \, d\Gamma = \mathbf{V}^T Q_{\text{in}}|_{S_d}, \tag{49}$$

with the vector $\mathbf{m}$ in the two-dimensional situations being defined as $\mathbf{m} = (1, 1, 0)^T$.

To solve these equations the time depended terms are approximated linearly as the difference between the current time step and the previous time step

$$\frac{\partial(\cdot)}{\partial t} = \frac{(\cdot)^{t+\Delta t} - (\cdot)^t}{\Delta t}, \tag{50}$$

where $(\cdot)^{t+\Delta t}$ is the unknown solution at the next time step, $(\cdot)^t$ is the known solution from the previous time step, and Δt is the length of the time step. The time independent terms are approximated by the weighted result of the current time step and the new time step:

$$(\cdot) = \bar{\theta}(\cdot)^{t+\Delta t} + (1-\bar{\theta})(\cdot)^t, \quad \bar{\theta} \in [0, 1]. \tag{51}$$

Stabilization is reached if $\bar{\theta} \geq \frac{1}{2}$. The Euler implicit time scheme is retrieved when $\bar{\theta} = 1$, while for $\bar{\theta} = 0$ the explicit Euler scheme is retrieved. Taking a short time step leads to initial oscillations. To have a stable time integration, the following criterion needs to be satisfied [33]

$$\Delta t > \frac{\Delta x^2}{ck}. \tag{52}$$

Here Δx is the element length and c is defined as $c = 2u + \lambda$.

The resulting system of equations is solved using a Newton–Raphson iterative method. Linearizing the aforementioned balance equations (Eqs. (45)–(49)), filling in the constitutive laws of Terzaghi effective stress (18), Darcy's law (20), and the leakage law (28), and including the spatial discretization (Eq. (41)) and time discretization (Eqs. (50) and (51)) we can write the final system

$$\begin{bmatrix} \mathbf{K}_{\hat{u}\hat{u}} & \mathbf{K}_{\hat{u}\tilde{u}} & \mathbf{C}_{\hat{u}\hat{p}} & \mathbf{C}_{\hat{u}\tilde{p}} & \mathbf{0} \\ \mathbf{K}_{\hat{u}\tilde{u}} & \mathbf{K}_{\tilde{u}\tilde{u}} & \mathbf{C}_{\tilde{u}\hat{p}} & \mathbf{C}_{\tilde{u}\tilde{p}} & \mathbf{Q}_{\tilde{u}p_d} \\ \mathbf{C}_{\hat{p}\hat{u}} & \mathbf{C}_{\hat{p}\tilde{u}} & \mathbf{D}_{\hat{p}\hat{p}} & \mathbf{D}_{\hat{p}\tilde{p}} & \mathbf{0} \\ \mathbf{C}_{\tilde{p}\hat{u}} & \mathbf{C}_{\tilde{p}\tilde{u}} & \mathbf{D}_{\tilde{p}\hat{p}} & \mathbf{D}_{\tilde{p}\tilde{p}} & \mathbf{0} \\ \mathbf{Q}_{p_d\hat{u}} & \mathbf{F}_{p_d\tilde{u}} & \bar{\theta}\Delta t\mathbf{Q}_{p_d\hat{p}} & \bar{\theta}\Delta t\mathbf{Q}_{p_d\tilde{p}} & \mathbf{F}_{p_dp_d} \end{bmatrix} \begin{bmatrix} \partial\hat{\mathbf{u}} \\ \partial\tilde{\mathbf{u}} \\ \partial\hat{\mathbf{p}} \\ \partial\tilde{\mathbf{p}} \\ \partial\mathbf{p_d} \end{bmatrix} = \begin{bmatrix} \mathbf{f}_{\hat{u}}^{\text{ext}} \\ \mathbf{f}_{\tilde{u}}^{\text{ext}} \\ \Delta t\mathbf{f}_{\hat{p}}^{\text{ext}} \\ \Delta t\mathbf{f}_{\tilde{p}}^{\text{ext}} \\ \Delta t\mathbf{f}_{p_d}^{\text{ext}} \end{bmatrix} - \begin{bmatrix} \mathbf{f}_{\hat{u}}^{\text{int}} \\ \mathbf{f}_{\tilde{u}}^{\text{int}} \\ \mathbf{f}_{\hat{p}}^{\text{int}} \\ \mathbf{f}_{\tilde{p}}^{\text{int}} \\ \mathbf{f}_{p_d}^{\text{int}} \end{bmatrix}. \tag{53}$$

The separate terms of the stiffness matrix are given in Appendix B. The external and internal force are defined as

$$\mathbf{f}_{\hat{u}}^{\text{ext}} = \int_{\Gamma_t} \mathbf{N}^T \mathbf{t}_{\text{p}}^{t+\Delta t} d\Gamma$$

$$\mathbf{f}_{\hat{u}}^{\text{int}} = \int_{\Omega_e} \mathbf{B}^T \boldsymbol{\sigma}_{j-1} d\Omega_e$$

$$\mathbf{f}_{\tilde{u}}^{\text{ext}} = \int_{\Gamma_t} \mathcal{H}_{\Gamma_d} \mathbf{N}^T \mathbf{t}_{\text{p}}^{t+\Delta t} d\Gamma$$

$$\mathbf{f}_{\tilde{u}}^{\text{int}} = \int_{\Omega_e} \mathcal{H}_{\Gamma_d} \mathbf{B}^T \boldsymbol{\sigma}_{j-1} d\Omega_e + \int_{\Gamma_d^+} h\mathbf{N}^T \{h\mathbf{t}_{d_{j-1}} - p_{d_{j-1}}\mathbf{n}_d\} d\Gamma$$

$$\mathbf{f}_{\hat{p}}^{\text{ext}} = \int_{\Gamma_q} \Delta t\mathbf{H}^T(\bar{\theta}q_{\text{p}}^{t+\Delta t} + (1-\bar{\theta})q_{\text{p}}^t) d\Gamma + \Delta t\mathbf{H}^T(\bar{\theta}q_{\Gamma}^{t+\Delta t} + (1-\bar{\theta})q_{\Gamma}^t)|_{S_d}$$

$$\begin{aligned} \mathbf{f}_{\hat{p}}^{\text{int}} = {} & \mathbf{C}_{\hat{p}\hat{u}} \cdot (\hat{\mathbf{u}}_{j-1}^{t+\Delta t} - \hat{\mathbf{u}}^t) + \mathbf{C}_{\hat{p}\tilde{u}} \cdot (\tilde{\mathbf{u}}_{j-1}^{t+\Delta t} - \tilde{\mathbf{u}}^t) + \Delta t\mathbf{K}_{\hat{p}\hat{p}} \cdot (\bar{\theta}\hat{\mathbf{p}}_{j-1}^{t+\Delta t} + (1-\bar{\theta})\hat{\mathbf{p}}^t) \\ & + \Delta t\mathbf{K}_{\hat{p}\tilde{p}} \cdot (\bar{\theta}\tilde{\mathbf{p}}_{j-1}^{t+\Delta t} + (1-\bar{\theta})\tilde{\mathbf{p}}^t) + \mathbf{M}_{\hat{p}\hat{p}} \cdot (\hat{\mathbf{p}}_{j-1}^{t+\Delta t} - \hat{\mathbf{p}}^t) + \mathbf{M}_{\hat{p}\tilde{p}} \cdot (\tilde{\mathbf{p}}_{j-1}^{t+\Delta t} - \tilde{\mathbf{p}}^t) \end{aligned}$$

$$\mathbf{f}_{\tilde{p}}^{\text{ext}} = \int_{\Gamma_q} \Delta t\mathcal{D}_{\Gamma_d}\mathbf{H}^T(\bar{\theta}q_{\text{p}}^{t+\Delta t} + (1-\bar{\theta})q_{\text{p}}^t) d\Gamma$$

$$\begin{aligned} \mathbf{f}_{\tilde{p}}^{\text{int}} = {} & \mathbf{C}_{\tilde{p}\hat{u}} \cdot (\hat{\mathbf{u}}_{j-1}^{t+\Delta t} - \hat{\mathbf{u}}^t) + \mathbf{C}_{\tilde{p}\tilde{u}} \cdot (\tilde{\mathbf{u}}_{j-1}^{t+\Delta t} - \tilde{\mathbf{u}}^t) + \Delta t\mathbf{K}_{\tilde{p}\hat{p}} \cdot (\bar{\theta}\hat{\mathbf{p}}_{j-1}^{t+\Delta t} + (1-\bar{\theta})\hat{\mathbf{p}}^t) \\ & + \Delta t(\mathbf{K}_{\tilde{p}\tilde{p}} + \mathbf{Q}_{\tilde{p}\tilde{p}}) \cdot (\bar{\theta}\tilde{\mathbf{p}}_{j-1}^{t+\Delta t} + (1-\bar{\theta})\tilde{\mathbf{p}}^t) + \mathbf{M}_{\tilde{p}\hat{p}} \cdot (\hat{\mathbf{p}}_{j-1}^{t+\Delta t} - \hat{\mathbf{p}}^t) + \mathbf{M}_{\tilde{p}\tilde{p}} \cdot (\tilde{\mathbf{p}}_{j-1}^{t+\Delta t} - \tilde{\mathbf{p}}^t) \end{aligned}$$

$$\mathbf{f}_{p_d}^{\text{ext}} = \mathbf{H}Q_{\text{in}}|_{S_d}$$

$$\begin{aligned} \mathbf{f}_{p_d}^{\text{int}} = {} & \mathbf{Q}_{p_d\hat{u}} \cdot (\hat{\mathbf{u}}_{j-1}^{t+\Delta t} - \hat{\mathbf{u}}^t) + (\mathbf{Q}_{p_d\tilde{u}}^{(1)} + \mathbf{Q}_{p_d\tilde{u}}^{(3)}) \cdot (\tilde{\mathbf{u}}_{j-1}^{t+\Delta t} - \tilde{\mathbf{u}}^t) + \Delta t\mathbf{Q}_{p_d\hat{p}} \cdot (\bar{\theta}\hat{\mathbf{p}}_{j-1}^{t+\Delta t} + (1-\bar{\theta})\hat{\mathbf{p}}^t) \\ & + \mathbf{Q}_{p_dp_d}^{(2)} \cdot (\mathbf{p}_{c_{j-1}}^{t+\Delta t} - \mathbf{p}_d^t) + \Delta t\mathbf{Q}_{p_dp_d}^{(3)} \cdot (\bar{\theta}\mathbf{p}_{c_{j-1}}^{t+\Delta t} + (1-\bar{\theta})\mathbf{p}_d^t) + \Delta t\bar{\theta}\frac{\delta\mathbf{H}}{\delta s}q_{t_{j-1}}^{t+\Delta t} + \Delta t(1-\bar{\theta})\frac{\delta\mathbf{H}}{\delta s}q_t^t \end{aligned}$$

with q_t being the component of the tangential fluid flow:

$$q_t = \frac{1}{12\mu} u_n^3 \frac{\partial \mathbf{H}^T}{\partial s} \mathbf{p}_d. \tag{54}$$

The numerical implementation and description is similar to the work of Remmers et al. [29,34,35]. The most important aspects are summarized in this section and the ELP implementation is described in more detail.

The nucleation and propagation of cohesive zones are based on the Camacho–Ortiz average stress criterion [36]. The averages stress is calculated by a Gaussian weighting function that is depended on a length scale parameter l_a. The nodes surrounding a discontinuity are enhanced the additional degrees of freedom. It is assumed that the discontinuity through an element is a straight line and always ends at the edge of the element. The fracture can grow through multiple elements in one time step. Numerical integration is performed with the standard Gaussian integration. Due to the arbitrary locations of the discontinuity the original integration points are not sufficient anymore. Therefore, the adopted integration scheme introduced by Wells and Sluys [22] is used for elements that are crossed by a discontinuity. The balance equation over the discontinuity are integrated by two integration points per element. The additional degree of freedom for the ELP model is carried by new nodes placed on the cross-points of the discontinuity and the element edge. These nodes only contribute to the one-dimensional pressure field in the discontinuity, see Fig. 4.

7. Examples

In this section we consider three examples. In the first two examples we use the ELP model but also a X-FEM model with a continuous pressure profile across the fracture. In the third example we only use the ELP model. For the details about the X-FEM model we refer to the work of Kraaijeveld et al. [25]. In the first example, we inject a constant volume in an opened fracture. With this example we illustrate the differences between the ELP and X-FEM model for the pressure in the fracture and the pressure profile at either sides of the fracture. In the second example, both models are compared with an analytical solution for hydraulic fracture propagation. In the third example we consider fracture nucleation and propagation from a circular hole. An implicit time scheme ($\theta = 1$) is used in both examples under two dimensional plane strain settings.

7.1. Fluid leakage from an opened fracture

In this example we benchmark the analytical leakage approximation (Eq. (28)) with the numerical models. Consider a column of rock formation with a horizontal traction free initial fracture in the middle of the column (Fig. 5(a)). The top and bottom surfaces of the column are both moved 0.01 mm away from the fracture creating a highly permeable fracture. The top and bottom fracture surfaces are then fixed in displacement and fluid is being injected with a constant rate $Q_{in} = 2.0\mathrm{e}^{-5} \frac{\mathrm{m}^2}{\mathrm{s}}$ at the left fracture entrance. We assume that the opened fracture is filled with fluid so that all injected fluid must leak into the rock formation. The rock formation has an intrinsic permeability $k_i = 1.0\mathrm{e}^{-20}$ m^2 and a fluid viscosity $\mu = 1.0\mathrm{e}^{-4}$ Pa s. The Young's modulus equals $E = 17.0$ GPa with a Poisson's ratio of $v = 0.2$. Both solid and fluid constituents are considered to be compressible with $K_s = 36.0$ GPa and $K_f = 3.0$ GPa. A time increment $\delta t = 0.01$ s is used in these simulations.

The consolidation distance of one time step can be approximated by $\Delta x_{crit} = \sqrt{(\Delta t E k)} = 0.13$ mm, where $k = k_i/\mu$ [37]. To resolve the pressure gradient it is necessary to use elements with an height lower than this consolidation distance. We violate this criterion deliberately by using elements with a height of 3.5 mm. In Fig. 5(b) we show that we can still predict the pressure in the fracture with the ELP model while the X-FEM model underestimates that fluid pressure. The pressure profile across the fracture for the X-FEM model at various times is shown in Fig. 6. It is clear that the pressure profile is not resolved in the X-FEM model, at early times (Fig. 6(a)), due to the large mesh size. This may lead to inaccurate results or numerical instabilities. At $t = 2.0$ s the consolidation distance is $\Delta x_{crit} = 1.8$ mm. Since the element at the fracture surface is divided in half, the consolidation distance is larger than the length over which the numerical integration takes place. In Fig. 6(b) it can be seen that indeed the X-FEM model can now resolve the pressure gradient on both sides of the fracture.

(a) Flow through a discontinuity.

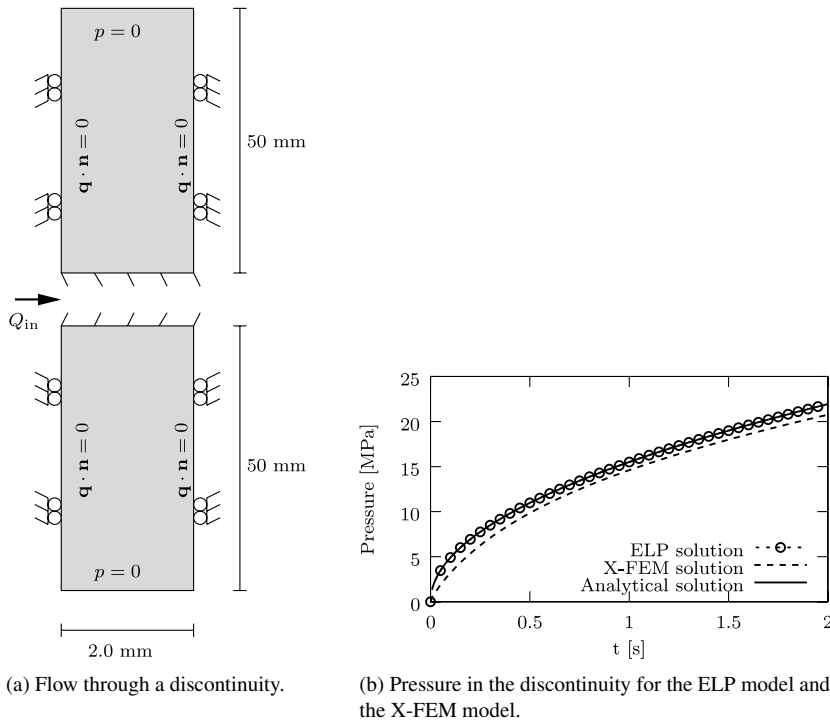(b) Pressure in the discontinuity for the ELP model and the X-FEM model.

Fig. 5. Schematic representation of the consolidation of a soil column due to flow through a discontinuity (a) and the result for the pressure in the discontinuity over the time (b).

(a) $t = 0.01$ s.

(b) $t = 2.0$ s.
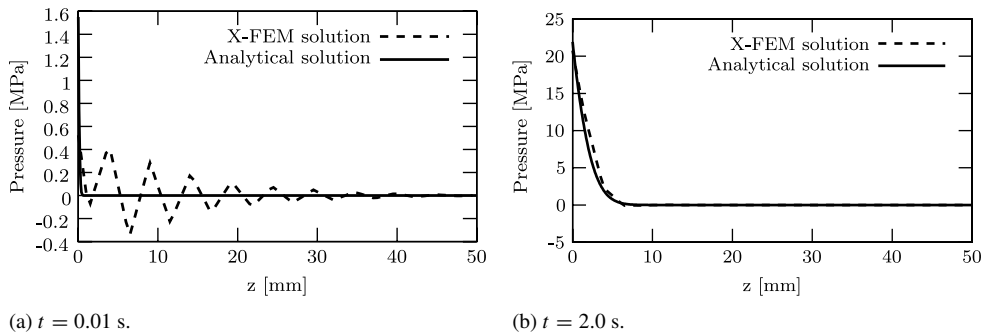
Fig. 6. Pressure for various times for the X-FEM model due to a constant fluid flow in the discontinuity.

7.2. KGD fracture problem

In this example, we analyse the KGD fracture problem as shown in Fig. 7 [7]. We consider a material with intrinsic permeability $k_i = 1.0e^{-18}$ m^2 and a fluid viscosity of $\mu = 1.0e^{-5}$ Pa s. The fracture toughness of the solid skeleton is taken as $\mathcal{G}_c = 120.0 \frac{N}{m}$ with an ultimate strength of $\tau_{ult} = 3.75$ MPa. The fluid injection rate $Q_{in} = 0.0005 \frac{m^2}{s}$ is assumed to be constant. The remainder of material properties and time discretization properties are equal to the previous example. The mesh near the fracture path is made of squared, 50.0×50.0 mm, elements. Again, a time step $\delta t = 0.01$ s is used.

Fig. 8 shows the pressure across the fracture with a single point indicating the pressure in fracture for the ELP model. It is not needed to resolve the pressure gradient caused by fluid leakage in the ELP model due to the analytical approximation of the pressure gradient. There are pressure oscillations near the fracture surface for the X-FEM model. Also, the pressure in the fracture simulated by X-FEM, is lower than in the rock formation. This leads to fluid being attracted into the fracture instead of fluid leakage to rock formation.

Fig. 7. Scheme of the KGD fracture problem.

Bunger et al. [38] derived an analytical solution for this type of fracture problem including fluid leak-off but neglecting any poroelastic effects in the bulk material. With the material properties the hydraulic fracture propagates in the storage dominated regime. The analytical solution approximates the fluid leak-off based with Carter's law [39]:
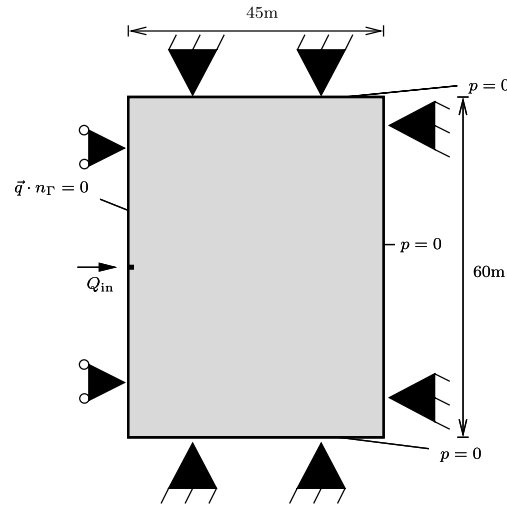
$$Q_{leakage} = \frac{2C_L}{\sqrt{t - t_0(x)}}, \tag{55}$$

where C_L is the leak-off coefficient, t is the current time, and t_0 is the time when the fracture arrived at position x. The leakage coefficient is an input parameter for the analytical solution and is therefore calculated by fitting equation (55) to the numerical leakage using the least squares method. The analytical solution is based a leakage coefficient of $C_l = 5.6e^{-6} \frac{m}{\sqrt{s}}$ calculated with the ELP solution. The comparison between the analytical solution and the numerical models is shown in Fig. 10. The leakage in the X-FEM model could not be fitted Carter's law. There is some discrepancy between the numerical models and the analytical solution. We attribute this to the differences between the numerical formation and the analytical solution. Namely, we describe the fracture process with a cohesive zone while the analytical solution is based on linear elastic fracture mechanics. Another significant difference is that the rock is linear elastic in the analytical solution but we include poro-elastic effects in the rock formation.

To illustrate the difference between the ELP and the X-FEM model we repeat the KGD fracture example with 4 different meshes. These meshes have a constant element size of $\ell_x = 20.0$ mm in the fracture direction. The mesh is refined in the y-direction, with a smallest element size of $\ell_y = 78.94$ mm. We validated that the numerical solution did not converge further using smaller elements. Therefore, we use this mesh as a reference solution. The reference solution is compared with 3 different meshes, having element sizes of $\ell_y = 100.0$ mm, $\ell_y = 166.6$ mm and $\ell_y = 300.0$ mm referred to as respectively, mesh 1, mesh 2 and mesh 3. The absolute error in the fracture length with respect to the reference solution for these 3 meshes is shown for the ELP model and the X-FEM model in respectively, Fig. 9(a) and (b). It is clear from these graphs that the error in the X-FEM models is larger and does not converge as fast to the reference solution as the ELP model.

7.3. Fracture from a circular hole

In the final example the ELP model is used to model a propagating fracture growing from a two-dimensional circular hole (Fig. 11). It assume that the confining stress $\sigma_0 = 1.25$ MPa in the y-direction is the half of the stress in the x-direction. We create two initial fractures, one perpendicular and one parallel to the highest confining stress. The fluid inflow $Q_{in} = 10.0 \frac{mm^2}{s}$ is constant and is distributed between the two fractures. Therefore, we assume that the fluid pressure is constant and equal in both fractures. The pressure at the fracture inlet is applied as a load on the circular wall to allow for deformations. The rock formation has an intrinsic permeability of $k_i = 1.0e^{-18}$ m^2 and a
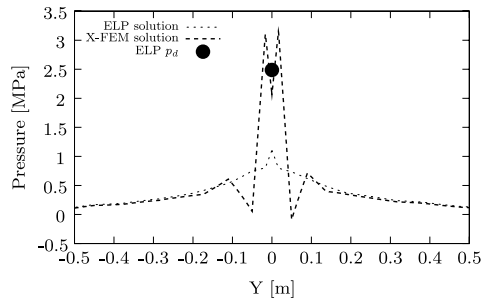
Fig. 8. Pressure distribution across the fracture for the ELP model and the X-FEM model. The black dot indicates pressure in the fracture for the ELP model.

(a) ELP solution.
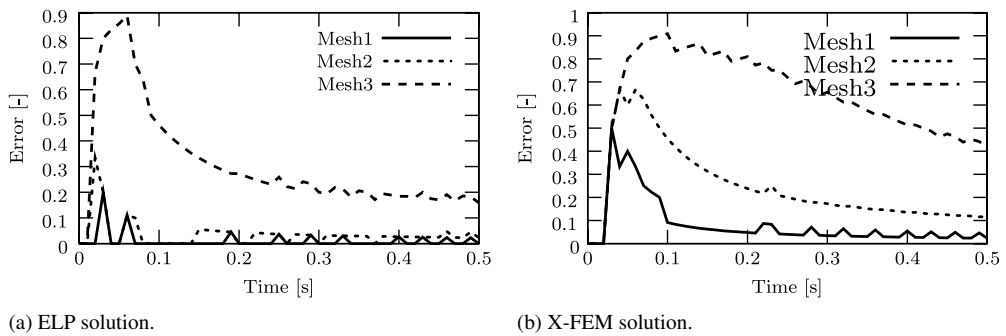
(b) X-FEM solution.

Fig. 9. Absolute error in the fracture length for the ELP and X-FEM models.

(a) Fracture length.

(b) Crack mouth opening.
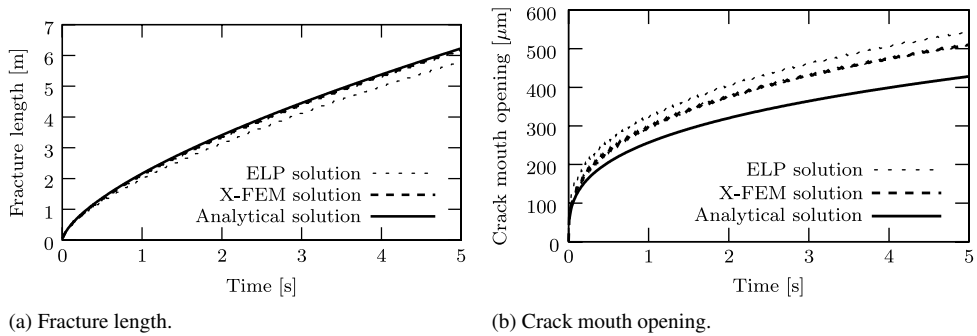
Fig. 10. The results of the numerical models and the analytical solution plotted against the time.
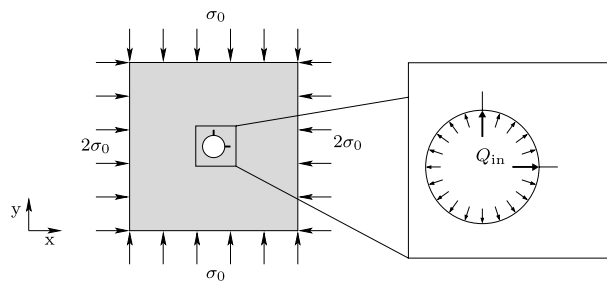
Fig. 11. Scheme of the borehole fracture problem.

(a) $t = 60$ s.

(b) $t = 600$ s.
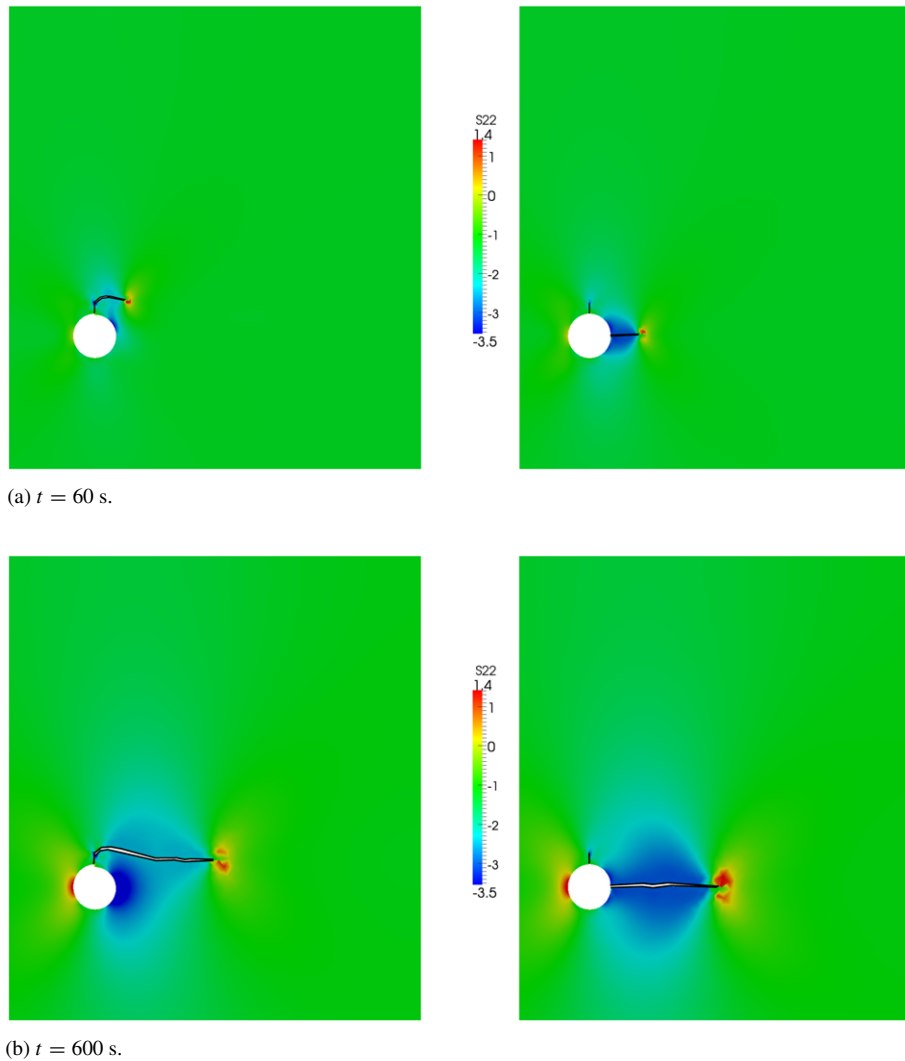
Fig. 12. Contour plots effective stress for the circular hole fracture problem. The deformed configuration is magnified 100 times. The results of the simulation with only one fracture in the y-direction are shown in the left column. The right column contains the results of the simulation with two fractures.

fluid viscosity of $\mu = 1.0\mathrm{e}^{-4}$ Pa s. The fracture toughness is taken as $\mathcal{G}_c = 120.0\ \frac{N}{m}$ and the ultimate strength as $\tau_{ult} = 1.25$ MPa. A time step of $\Delta t = 6.0$ s is used. The remainder of material properties are again the same as the first example.

The initial stress concentration has been validated with Kirsch's analytical solution [40]. From experimental measurements it is known that the preferred propagation direction of a hydraulic fracture is perpendicular to the minimum confining stress [41]. To illustrate this we also perform the simulation with only the initial fracture in the y-direction. The results of these two simulations can be seen in Fig. 12. In the left column it is shown that the fracture indeed turns in the direction of minimum confining stress. In the situation of two fractures (right column), only the fracture that is initially already perpendicular to the minimum confining stress propagates. This is expected as it costs less energy to grow the fracture in this direction. At the left side of the circular hole stress is being generated due to the loading of the circular wall.

In the next simulation we do consider the possibility of fracture nucleation. We start the simulation with only the initial fracture perpendicular to the highest confining stress (Fig. 13(a)). The stress generated at both sides of the circular hole leads to the nucleation of two new fractures (Fig. 13(b)).

(a) $t = 12$ s.   (b) $t = 282$ s.

Fig. 13. Contour plots of the effective stress for the circular hole. The deformed configuration is magnified 100 times. In the left figure, the situation before fracture nucleation is shown. In the right figure, the two nucleated fractures in preferential fracture direction are shown.

8. Conclusion

We have presented an enhanced local pressure model, within the framework of X-FEM, for fluid pressure driven fracture in porous saturated materials. By exploiting the partition-of-unity property of finite element shape functions the method captures the discontinuous fracture. The fract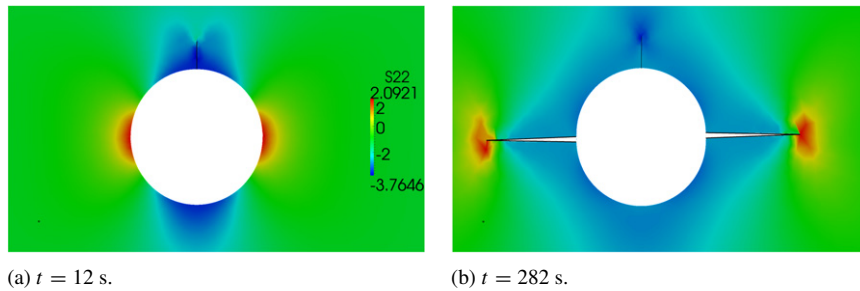ure process is modelled by means of a cohesive zone description. The local, additional, degree of freedom for the pressure ensures that fluid flow goes exclusively in the fracture. The steep pressure gradient that may occur locally near the fracture surface is reconstructed based on Terzaghi's analytical solution.

We have illustrated this effect with an example where fluid is being injected in an opened fracture. Using a X-FEM model with a continuous pressure approach the pressure gradient cannot be resolved at low time scales. The pressure in the fracture calculated with the ELP model is consistent with the analytical solution. We also have showed that at higher time scales the continuous X-FEM does describe the pressure gradient near the fracture surface. This indicates that the ELP model is better capable to model hydraulic fracturing at early stages while at later stages a switch to the continuous X-FEM should be considered.

In the second example we have compared the propagation of a hydraulic fracture under a constant fluid injection with an analytical solution in the storage dominated regime. The trend of the ELP model is comparable to the analytical solution. We attribute this due to the fact that the analytical solution is based on different assumptions such as linear elastic fracture mechanics and that poro-elastic effects in the rock formation are neglected. We also showed with a mesh refinement study that the ELP model converges the reference solution faster than the X-FEM model.

In the last example we have considered fracture propagation from a circular hole that can deform depending on the pressure in fracture. Here we have showed that the fracture can grow in arbitrary propagation angles. The fracture propagated in the direction parallel to the highest confining stress. This behaviour is energetically favourable and is also in agreement with experimental data. In this example we have also included fracture nucleation. As expected the fractures nucleated in the plane of lowest confining stress.

Based on our results we conclude that the ELP model has significant advantages compared to the continuous X-FEM model in hydraulic fracturing of low permeable rock formations such as shales. Fluid can be injected exclusively in the fractures and it is not necessary to have a dense mesh to resolve the pressure gradient near the fracture.

Acknowledgements

Appendix A

In this appendix we will solve Terzaghi's one dimensional consolidation equation [28] for two different boundary conditions. First, we look at the consolidation of a soil layer under load. Secondly, we look at a soil column under the

injection of a constant fluid flow. This is comparable to the early stages of hydraulic fracturing. The one dimensional consolidation equation is given by

$$\frac{\partial p}{\partial t} = c_v \frac{\partial^2 p}{\partial x^2} \tag{56}$$

where c_v is the diffusion coefficient and is given by

$$c_v = kM \frac{K + \frac{4}{3}\mu}{K_u + \frac{4}{3}\mu}. \tag{57}$$

Here K and μ are the bulk modulus and the shear modulus, respectively. The undrained bulk modulus is defined as

$$K_u = K + \alpha^2 M. \tag{58}$$

Using separation of variables we can derive the well known 1D consolidation equation:

$$p(z, t) = \frac{2p_0}{h} \sum_{i=1}^{\infty} \frac{1}{\mu_i} e^{-\lambda_i c_v t} \sin(\mu_i z). \tag{59}$$

Here is p_0 the applied load, h is the height of the soil layer, z is the coordinate system along the height of the consolidation column, and λ_i and μ_i are summation constants defined by

$$\lambda_i = \mu_i^2 = \left(\frac{(2i-1)\pi}{2h} \right)^2. \tag{60}$$

Changing the bottom boundary condition to a constant fluid flow Q_{in} results in the following equation for the pressure

$$p(z, t) = -\frac{Q_{in}}{k} z + \frac{Q_{in}}{k} h - \frac{2Q_{in}}{hk} \sum_{i=1}^{\infty} \frac{1}{\mu_i^2} e^{-\lambda_i c_v t} \cos(\mu_i z). \tag{61}$$

Since the latter solution is depended on the height of the soil layer we also give the solution for an semi-infinite soil layer

$$\frac{2Q_{in}}{k} \left(\sqrt{\frac{c_v t}{\pi}} \exp \frac{-\eta^2}{4c_v t} - \frac{\eta}{2} \text{erfc} \left(\frac{\eta}{2\sqrt{c_v t}} \right) \right). \tag{62}$$

Here η is the distance form the discontinuity to a point the formation. This equation was derived for the flux of heat through a semi-infinite solid by Carslaw and Jaeger [42].

Appendix B

The element matrices are divided in four categories:
The stiffness matrices:

$$\mathbf{K}_{\hat{u}\hat{u}} = \int_{\Omega_e} \mathbf{B}^T \mathbf{DB} \mathrm{d}\Omega_e \qquad \mathbf{K}_{\hat{u}\tilde{u}} = \int_{\Omega_e} \mathcal{H}_{\Gamma_d} \mathbf{B}^T \mathbf{DB} \mathrm{d}\Omega_e$$

$$\mathbf{K}_{\tilde{u}\tilde{u}} = \int_{\Omega_e} \mathcal{H}_{\Gamma_d}^2 \mathbf{B}^T \mathbf{DB} \mathrm{d}\Omega_e + \int_{\Gamma_d^+} h^2 \mathbf{N}^T \mathbf{TN} \mathrm{d}\Gamma$$

$$\mathbf{K}_{\hat{p}\hat{p}} = -\int_{\Omega_e} k \nabla \mathbf{H}^T \nabla \mathbf{H} \mathrm{d}\Omega_e \qquad \mathbf{K}_{\hat{p}\tilde{p}} = -\int_{\Omega_e} k \mathcal{H}_{\Gamma_d}^s \nabla \mathbf{H}^T \nabla \mathbf{H} \mathrm{d}\Omega_e$$

$$\mathbf{K}_{\tilde{p}\hat{p}} = -\int_{\Omega_e} k \mathcal{H}_{\Gamma_d}^s \nabla \mathbf{H}^T \nabla \mathbf{H} \mathrm{d}\Omega_e \qquad \mathbf{K}_{\tilde{p}\tilde{p}} = -\int_{\Omega_e} k (\mathcal{H}_{\Gamma_d}^s)^2 \nabla \mathbf{H}^T \nabla \mathbf{H} \mathrm{d}\Omega_e$$

the mass matrices:

$$\mathbf{M}_{\hat{p}\hat{p}} = -\int_{\Omega_e} \frac{1}{M}\mathbf{H}^T\mathbf{H}\mathrm{d}\Omega_e \qquad \mathbf{M}_{\hat{p}\tilde{p}} = -\int_{\Omega_e} \frac{1}{M}\mathcal{H}^s_{\Gamma_d}\mathbf{H}^T\mathbf{H}\mathrm{d}\Omega_e$$

$$\mathbf{M}_{\tilde{p}\hat{p}} = -\int_{\Omega_e} \frac{1}{M}\mathcal{H}^s_{\Gamma_d}\mathbf{H}^T\mathbf{H}\mathrm{d}\Omega_e \qquad \mathbf{M}_{\tilde{p}\tilde{p}} = -\frac{1}{M}(\mathcal{H}^s_{\Gamma_d})^2\mathbf{H}^T\mathbf{H}\mathrm{d}\Omega_e$$

the coupling matrices

$$\mathbf{C}_{\hat{u}\hat{p}} = -\alpha\int_{\Omega_e}\mathbf{B}^T(\mathbf{mH})\mathrm{d}\Omega_e \qquad \mathbf{C}_{\hat{u}\tilde{p}} = -\alpha\int_{\Omega_e}\mathcal{H}^s_{\Gamma_d}\mathbf{B}^T(\mathbf{mH})\mathrm{d}\Omega_e$$

$$\mathbf{C}_{\tilde{u}\hat{p}} = -\alpha\int_{\Omega_e}\mathcal{H}_{\Gamma_d}\mathbf{B}^T(\mathbf{mH})\mathrm{d}\Omega_e \qquad \mathbf{C}_{\tilde{u}\tilde{p}} = -\alpha\int_{\Omega_e}\mathcal{H}_{\Gamma_d}\mathcal{H}^s_{\Gamma_d}\mathbf{B}^T(\mathbf{mH})\mathrm{d}\Omega_e$$

$$\mathbf{C}_{\hat{p}\hat{u}} = -\alpha\int_{\Omega_e}\mathbf{H}^T\mathbf{m}^T\mathbf{B}\mathrm{d}\Omega_e \qquad \mathbf{C}_{\hat{p}\tilde{u}} = -\alpha\int_{\Omega_e}\mathcal{H}_{\Gamma_d}\mathbf{H}^T\mathbf{m}^T\mathbf{B}\mathrm{d}\Omega_e$$

$$\mathbf{C}_{\tilde{p}\hat{u}} = -\alpha\int_{\Omega_e}\mathcal{H}^s_{\Gamma_d}\mathbf{H}^T\mathbf{m}^T\mathbf{B}\mathrm{d}\Omega_e \qquad \mathbf{C}_{\tilde{p}\tilde{u}} = -\alpha\int_{\Omega_e}\mathcal{H}_{\Gamma_d}\mathcal{H}^s_{\Gamma_d}\mathbf{H}^T\mathbf{m}^T\mathbf{B}\mathrm{d}\Omega_e$$

and the crack flow terms

$$\mathbf{Q}_{\tilde{u}p_d} = -\int_{\Gamma_d^+} h\mathbf{N}^T\mathbf{n}_d\mathbf{V}\mathrm{d}\Gamma \qquad \mathbf{Q}^{(2)}_{p_d\tilde{u}} = \int_{\Gamma_d}\frac{3}{12\mu}\frac{\partial\mathbf{V}^T}{\partial s}\frac{\partial\mathbf{V}}{\partial s}\mathbf{p}_d u_n^2 h\mathbf{n}_d^T\mathbf{N}\mathrm{d}\Gamma$$

$$\mathbf{Q}_{p_dp_d} = \int_{\Gamma_d}\frac{1}{12\mu}\frac{\partial\mathbf{V}^T}{\partial s}u_n^3\frac{\partial\mathbf{V}}{\partial s}\mathrm{d}\Gamma \qquad \mathbf{Q}_{p_d\hat{p}} = -2C_a\int_{\Gamma_d}\mathbf{V}^T\mathbf{H}\mathrm{d}\Gamma$$

$$\mathbf{Q}_{p_d\hat{u}} = \int_{\Gamma_d}u_n\mathbf{V}^T\mathbf{t}^T\frac{\partial\mathbf{N}}{\partial s}\mathrm{d}\Gamma \qquad \mathbf{Q}^{(3)}_{p_d\tilde{u}} = \int_{\Gamma_d}\frac{1}{2}u_n\mathbf{V}^T\mathbf{t}^T\frac{\partial\mathbf{N}}{\partial s}\mathrm{d}\Gamma$$

$$\mathbf{Q}^{(2)}_{p_dp_d} = \int_{\Gamma_d}\frac{u_n}{K_f}\mathbf{V}^T\mathbf{V}\dot{\mathbf{p}}_d\mathrm{d}\Gamma \qquad \mathbf{Q}^{(1)}_{p_d\tilde{u}} = \int_{\Gamma_d}h\mathbf{V}^T\mathbf{n}_d\mathbf{N}\mathrm{d}\Gamma$$

$$\mathbf{Q}^{(3)}_{p_dp_d} = 2C_a\int_{\Gamma_d}\mathbf{V}\mathbf{V}^T\mathrm{d}\Gamma \qquad \mathbf{Q}_{p_d\tilde{p}} = -2C_a\int_{\Gamma_d}\mathbf{V}^T\mathbf{V}\mathrm{d}\Gamma.$$

The additional terms in the stiffness matrix are defined by

$$\mathbf{D}_{\hat{p}\hat{p}} = \bar{\theta}\Delta t\mathbf{K}_{\hat{p}\hat{p}} + \mathbf{M}_{\hat{p}\hat{p}} \qquad \mathbf{D}_{\hat{p}\tilde{p}} = \bar{\theta}\Delta t\mathbf{K}_{\hat{p}\hat{p}} + \mathbf{M}_{\hat{p}\tilde{p}}$$

$$\mathbf{D}_{\tilde{p}\hat{p}} = \bar{\theta}\Delta t\mathbf{K}_{\hat{p}\hat{p}} + \mathbf{M}_{\hat{p}\hat{p}} \qquad \mathbf{D}_{\tilde{p}\tilde{p}} = \bar{\theta}\Delta t\mathbf{K}_{\tilde{p}\tilde{p}}$$

$$\mathbf{F}_{p_d\tilde{u}} = \mathbf{Q}^{(1)}_{p_d\tilde{u}} + \bar{\theta}\Delta t\mathbf{Q}^{(2)}_{p_d\tilde{u}} + \mathbf{Q}^{(3)}_{p_d\tilde{u}} \qquad \mathbf{F}_{p_dp_d} = \bar{\theta}\Delta t(\mathbf{Q}_{p_dp_d} + \mathbf{Q}^{(3)}_{p_dp_d}) + \mathbf{Q}^{(2)}_{p_dp_d}.$$

The derivative of $\mathbf{N}$ in the tangential direction of the fracture is calculated as follows:

$$\mathbf{t}^T\frac{\partial\mathbf{N}^T}{\partial s} = \mathbf{t}^T\nabla\mathbf{N}^T\mathbf{W}\mathbf{M}, \tag{63}$$

with $\mathbf{W}$ being the following support matrix in the case of four nodal elements

$$\mathbf{W} = \begin{pmatrix} 1 & 1 & 0 & 0 & 0 & 0 & 0 & 0 \\ 1 & 1 & 0 & 0 & 0 & 0 & 0 & 0 \\ 0 & 0 & 1 & 1 & 0 & 0 & 0 & 0 \\ 0 & 0 & 1 & 1 & 0 & 0 & 0 & 0 \\ 0 & 0 & 0 & 0 & 1 & 1 & 0 & 0 \\ 0 & 0 & 0 & 0 & 1 & 1 & 0 & 0 \\ 0 & 0 & 0 & 0 & 0 & 0 & 1 & 1 \\ 0 & 0 & 0 & 0 & 0 & 0 & 1 & 1 \end{pmatrix}, \tag{64}$$

and **M** being a support matrix containing the contributions of the tangent vector on its diagonal

$$M = \text{diag}\left[\mathbf{t}_x, \mathbf{t}_y, \mathbf{t}_x, \mathbf{t}_y, \mathbf{t}_x, \mathbf{t}_y, \mathbf{t}_x, \mathbf{t}_y\right].$$

(65)

References

[1] J. Adachi, E. Siebrits, A. Peirce, J. Desroches, Computer simulation of hydraulic fractures, Int. J. Rock Mech. Min. Sci. 44 (5) (2007) 739–757.
[2] B. Legarth, E. Huenges, G. Zimmermann, Hydraulic fracturing in a sedimentary geothermal reservoir: results and implications, Int. J. Rock Mech. Min. Sci. 42 (7) (2005) 1028–1041.
[3] J. Desroches, E. Detournay, B. Lenoach, P. Papanastasiou, J. Pearson, M. Thiercelin, A. Cheng, The crack tip region in hydraulic fracturing, Proc. R. Soc. A 447 (1929) (1993) 39–48.
[4] J. Adachi, E. Detournay, Plane strain propagation of a hydraulic fracture in a permeable rock, Eng. Fract. Mech. 75 (16) (2008) 4666–4694.
[5] T. Perkins, L. Kern, Widths of hydraulic fractures, J. Pet. Technol. 13 (9) (1961) 937–949.
[6] R. Nordgren, Propagation of a vertical hydraulic fracture, Old SPE J. 12 (4) (1972) 306–314.
[7] J. Geertsma, F. De Klerk, A rapid method of predicting width and extent of hydraulically induced fractures, J. Pet. Technol. 21 (12) (1969) 1571–1581.
[8] S. Khristianovic, Y. Zheltov, Formation of vertical fractures by means of highly viscous liquid, in: Proceedings of the Fourth World Petroleum Congress, Rome, 1955 pp. 579–586.
[9] T. Boone, A. Ingraffea, A numerical procedure for simulation of hydraulically-driven fracture propagation in poroelastic media, Int. J. Numer. Anal. Methods Geomech. 14 (1) (1990) 27–47.
[10] B. Schrefler, S. Secchi, L. Simoni, On adaptive refinement techniques in multi-field problems including cohesive fracture, Comput. Methods Appl. Mech. Engrg. 195 (4) (2006) 444–461.
[11] S. Secchi, L. Simoni, B. Schrefler, Mesh adaptation and transfer schemes for discrete fracture propagation in porous materials, Int. J. Numer. Anal. Methods Geomech. 31 (2) (2007) 331–345.
[12] S. Secchi, B. Schrefler, A method for 3D hydraulic fracturing simulation, Int. J. Fract. (2012) 1–14.
[13] E. Sarris, P. Papanastasiou, The influence of the cohesive process zone in hydraulic fracturing modelling, Int. J. Fract. 167 (1) (2011) 33–45.
[14] J. Segura, I. Carol, On zero-thickness interface elements for diffusion problems, Int. J. Numer. Anal. Methods Geomech. 28 (9) (2004) 947–962.
[15] J. Segura, I. Carol, Coupled HM analysis using zero-thickness interface elements with double nodes. Part I: theoretical model, Int. J. Numer. Anal. Methods Geomech. 32 (18) (2008) 2083–2101.
[16] B. Carrier, S. Granet, Numerical modeling of hydraulic fracture problem in permeable medium using cohesive zone model, Eng. Fract. Mech. 79 (2012) 312–328.
[17] M. Wheeler, T. Wick, W. Wollner, An augmented-Lagrangian method for the phase-field approach for pressurized fractures, Comput. Methods Appl. Mech. Engrg. 271 (2014) 69–85.
[18] J. Remmers, R. De Borst, A. Needleman, A cohesive segments method for the simulation of crack growth, Comput. Mech. 31 (1–2) (2003) 69–77.
[19] J. Melenk, I. Babuška, The partition of unity finite element method: basic theory and applications, Comput. Methods Appl. Mech. Engrg. 139 (1) (1996) 289–314.
[20] T. Belytschko, T. Black, Elastic crack growth in finite elements with minimal remeshing, Internat. J. Numer. Methods Engrg. 45 (5) (1999) 601–620.
[21] N. Moës, J. Dolbow, T. Belytschko, A finite element method for crack growth without remeshing, Internat. J. Numer. Methods Engrg. 46 (1) (1999) 131–150.
[22] G. Wells, L. Sluys, A new method for modelling cohesive cracks using finite elements, Internat. J. Numer. Methods Engrg. 50 (12) (2001) 2667–2682.
[23] F. Irzal, J. Remmers, J. Huyghe, R. de Borst, A large deformation formulation for fluid flow in a progressively fracturing porous material, Comput. Methods Appl. Mech. Engrg. 256 (2013) 29–37.
[24] R. De Borst, J. Réthoré, M. Abellan, A numerical approach for arbitrary cracks in a fluid-saturated medium, Arch. Appl. Mech. 75 (10) (2006) 595–606.
[25] F. Kraaijeveld, J. Huyghe, J. Remmers, R. de Borst, 2D mode I crack propagation in saturated ionized porous media using partition of unity finite elements, J. Appl. Mech. 80 (2) (2013) 020907.
[26] T. Mohammadnejad, A. Khoei, Hydro-mechanical modeling of cohesive crack propagation in multiphase porous media using the extended finite element method, Int. J. Numer. Anal. Methods Geomech. 37 (10) (2012) 1247–1279.
[27] T. Mohammadnejad, A. Khoei, An extended finite element method for hydraulic fracture propagation in deformable porous media with the cohesive crack model, Finite Elem. Anal. Des. 73 (2013) 77–95.
[28] K. Terzaghi, Theoretical Soil Mechanics, J. Wiley, New York, 1943.
[29] J. Remmers, R. de Borst, A. Needleman, The simulation of dynamic crack propagation using the cohesive segments method, J. Mech. Phys. Solids 56 (1) (2008) 70–92.
[30] P. Witherspoon, J. Wang, K. Iwai, J. Gale, Validity of cubic law for fluid flow in a deformable rock fracture, Water Resour. Res. 16 (6) (1980) 1016–1024.
[31] M. Biot, General theory of three-dimensional consolidation, J. Appl. Phys. 12 (2) (1941) 155–164.
[32] F. Kraaijeveld, J. Huyghe, Propagating cracks in saturated ionized porous media, Multiscale Meth. Comput. Mech. (2011) 425–442.
[33] F. Kraaijeveld, Propagating discontinuities in ionized porous media (Ph.D. thesis), Technische Universiteit Eindhoven, 2009.
[34] J. Remmers, Discontinuities in materials and structures (Ph.D. thesis), Delft University of Technology, 2006.

[35] E. Remij, J. Remmers, F. Pizzocolo, D. Smeulders, J. Huyghe, A partition of unity-based model for crack nucleation and propagation in porous media, including orthotropic materials, Transp. Porous Media (2015). http://dx.doi.org/10.1007/s11242-014-0399-z. in press.

[36] G. Camacho, M. Ortiz, Computational modelling of impact damage in brittle materials, Internat J. Solids Struct. 33 (20) (1996) 2899–2938.

[37] P. Vermeer, A. Verruijt, An accuracy condition for consolidation by finite elements, Int. J. Numer. Anal. Methods Geomech. 5 (1) (1981) 1–14.

[38] A. Bunger, E. Detournay, D. Garagash, Toughness-dominated hydraulic fracture with leak-off, Int. J. Fract. 134 (2) (2005) 175–190.

[39] G. Howard, C. Fast, Optimum fluid characteristics for fracture extension, Drilling and Production Practice.

[40] G. Kirsch, Die Theorie der Elastizität und die Bedürfnisse der Festigkeitslehre, Z. Ver. Dtsch. Ing. 42 (1898) 797–807.

[41] M. Rahman, M. Hossain, D. Crosby, M. Rahman, S. Rahman, Analytical, numerical and experimental investigations of transverse fracture propagation from horizontal wells, J. Pet. Sci. Eng. 35 (3) (2002) 127–150.

[42] H. Carslaw, J. Jaeger, Heat in Solids, Vol. 19591, Clarendon Press, Oxford, 1959.